# Simulation of erosion by a particulate airflow through a ventilator

**A Ghenaiet**

Faculty of Mechanical and Process Engineering, University of Sciences and Technology, USTHB, BP32 El-Alia, Bab-ezzouar, 16111, Algiers, Algeria

E-mail: ag1964@yahoo.com

**Abstract.** Particulate flows are a serious problem in air ventilation systems, leading to erosion of rotor blades and aerodynamic performance degradation. This paper presents the numerical results of sand particle trajectories and erosion patterns in an axial ventilator and the subsequent blade deterioration. The flow field was solved separately by using the code CFX-TASCflow. The Lagrangian approach for the solid particles tracking implemented in our in-house code considers particle and eddy interaction, particle size distribution, particle rebounds and near walls effects. The assessment of erosion wear is based on the impact frequency and local values of erosion rate. Particle trajectories and erosion simulation revealed distinctive zones of impacts with high rates of erosion mainly on the blade pressure side, whereas the suction side is eroded around the leading edge.

## 1. Introduction

The ingestion of dust particles by air compressors and ventilation systems is inevitable and results in drastic degradations of their aerodynamic performance and structural integrity. The quartz is the most abundant erosive constituent and its abrasive impacts provoke a considerable erosion wear near the leading edge and tip of axial blades [1]. Measurements by Balan and Tabakoff [2] in an isolated axial compressor that followed erosion cycles indicated a reduction in compressor adiabatic efficiency and stage loading and a severe erosion of blade leading edge and pressure side with increased roughness. Ghenaiet et al. [3] characterized the increase in tip clearance and the reduction of blade chord of a high speed conta-whirl axial fan rotating at 11000 rpm, and noticed 7.1 % and 9.5 % drop in efficiency and pressure rise coefficient, respectively, after 9 hours of sand ingestion. Experimental procedures to assess erosion and performance degradation remain very expensive and reveal limited information because of different operating conditions of a turbomachine; subsequently the numerical simulations are a good alternative. Hussein and Tabakoff [4] pioneered in the particle trajectory simulations through the axial flow turbomachines and the use of experimentally based particle rebound factors. Ghenaiet et al. [5] presented a complete numerical procedure for simulating particle trajectory, erosion and the subsequent aerodynamic performance degradation, which was validated upon a contra-whirl axial fan stage consisting of seven IGVs and ten twisted rotor blades operating at a speed of 11000 rpm. In other simulations carried out by Ghenaiet [6] for a larger axial fan stage operating at a speed of 4650 rpm, results have shown that for different positions of rotor blade the main impacted areas are seen over the blade leading edge corner and the pressure side towards the tip, in addition to a strip over

the suction side. In radial compressors the computations of trajectories carried out by Ghenaiet [7], have shown that are consistently different from those in axial turbomachinery, because of flow structure and direction of Coriolis and centrifugal force, and there are distinctive zones of high rates of erosion and the blade pressure side is more eroded. The prediction of erosion in turbomachinery is still a very difficult task due to several involved factors including; initial location of rotor blade, flow conditions, random particle size distribution and uncertainties in initial particle locations and impacting conditions. This paper presents the results of particle trajectories through an axial ventilator and the subsequent blade erosion. The trajectory and erosion computations used our developed Lagrangian tracking code which has been validated and used in previous studies [3, 5-7]. The studied ventilator is manufactured by Woods and rotates at a fixed speed of 1440 rpm. The rotor made from aluminium (figure 1) has seven highly staggered (root stagger 73 deg and tip stagger 82 deg) C4 blades of a maximum chord length 117.5 mm. The tip diameter is 479.6 mm and the hub diameter is 156.5 mm. A test-rig was used to measure the characteristics (figure 2) that depicts the stable and instable branches of pressure rise and the maximum efficiency occurring near full opening. It was not possible going beyond a flow rate of 1 $m^3/s$ due to throttling.

**Figure 1.** Axial fan Woods

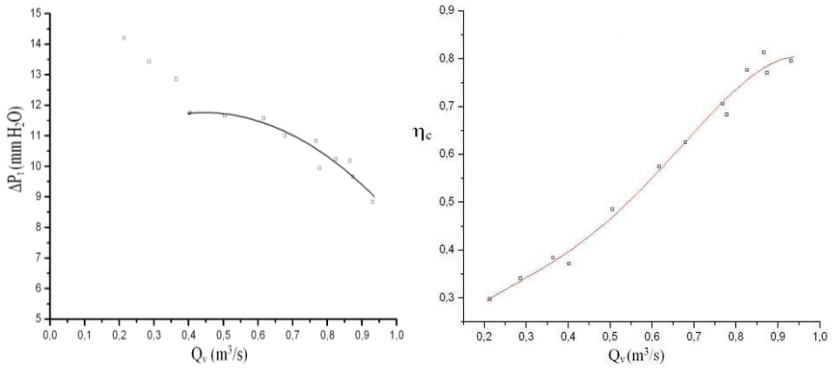


**Figure 2.** Measured characteristics, (left) Pressure rise, (right) Isentropic efficiency

## 2. Gas path computations

The flow-field was computed separately from solid phase by means of the time averaging Navier-Stokes solver TASCflow. The computational domain in addition to the rotor blade contains an extended hub housing the motor, inlet and outlet sector with a step transition, as shown by figure 3.

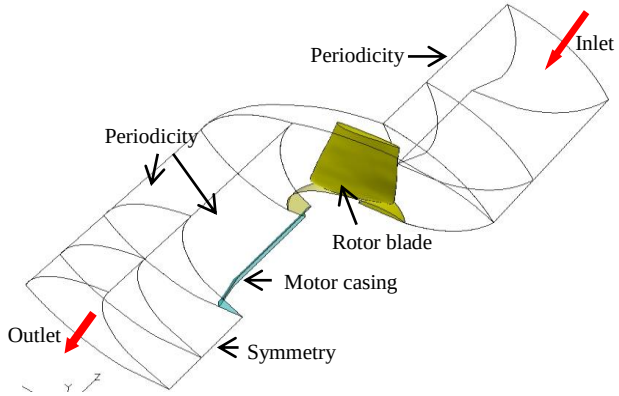


**Figure 3.** Computational domain

The computational mesh is of an H type as shown for the hub to shroud and for blade to blade (figure 4). A fine grid is attached to the tip-clearance region and a fine clustering is used near the walls. The six sub-grids are attached using stages interfaces.
The boundary conditions used are: a constant total pressure at the inlet and a mass flow at the outlet. Periodic boundaries are applied at one pitch of the rotor blades, at the hub and the extended domains which are joining on the axis of rotation, where a symmetry boundary condition is applied. In these CFD simulations the blade root stagger angles was set at 73°, and the mass flow rate corresponded to maximum opening.

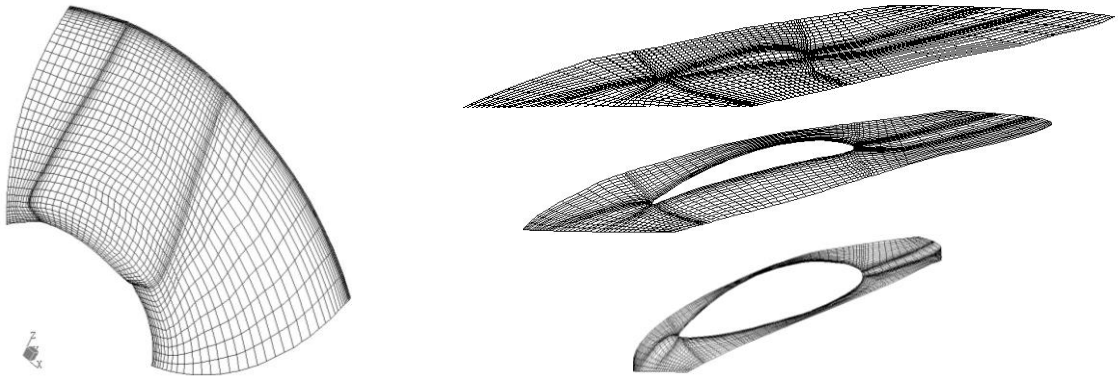

**Figure 4:** Rotor grid: **a)** Hub to shroud **b)** hub, mid-span and tip

Figure 5 shows the flow velocity vectors plotted near the hub, mid span and in tip clearance for. Upstream and around the blade leading edge the relative flow velocities are relatively high and increasing with the blade height. At the trailing edge of fan blade there is evidence of wake formation, which is also clear from total relative pressure (plot not shown). The most complex flow features occur in the tip clearance region, where the leakage around the blade tip develops into a vortex and mixes out with the annulus wall boundary layer, thus increasing losses. The flow at rotor exit is strongly influenced by the back-pressure at the rotor step, where a strong diffusion occurs, and the amount of flow rotation tends to reduce after nearly two diameters distance.

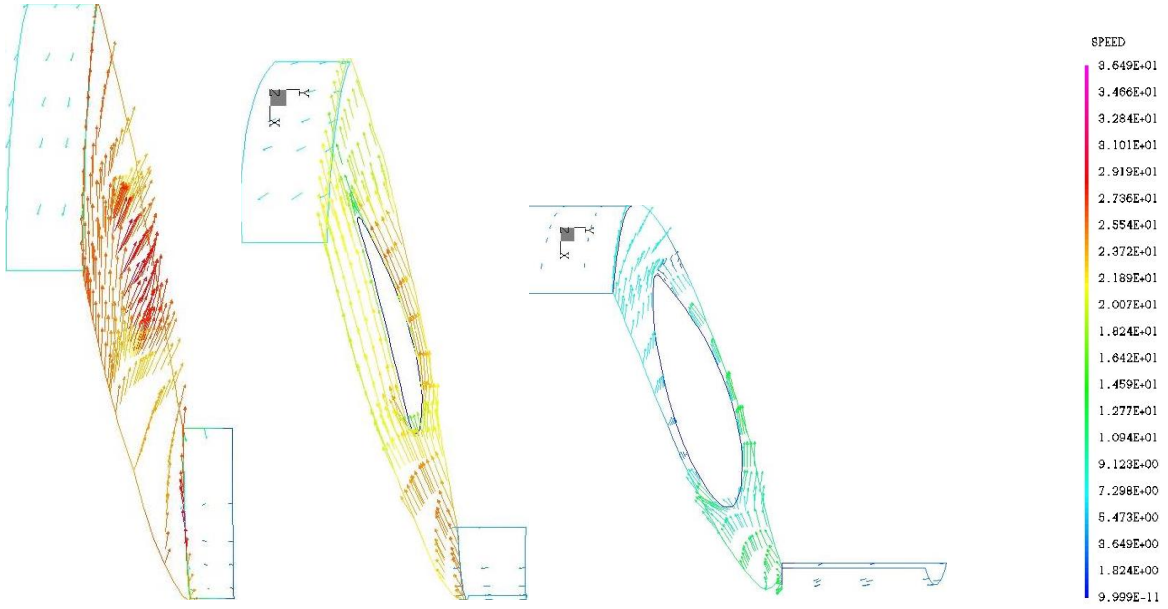


**Figure 5.** Velocity vectors near hub, mid and tip, at maximum opening

## 3. Particle trajectories and erosion computation

The Lagrangian approach considers the tracking of individual particles from different starting positions, thus giving an ability to handle in more details some physical aspects, such as the interaction with walls. This approach is preferred since the effect of particle phase on flow solution is neglected as the volume fraction is less than the upper limit of $10^{-6}$ [8].

The particle trajectory equations are derived from the superposition of different involved forces, but in most particulate air flows the drag force is dominant. The general expression for the drag coefficient is given as below according to Haider and Levenspiel [9], for Reynolds number from 0.01 to $2.6\text{x}10^5$. For small Reynolds numbers Re<0.5 the viscous effect is dominating and this is referred as the Stokes regime $C_D=24/Re$ and this value is used. The constants A, B, C and D depend on the particle shape.

$$\vec{F}_D = \frac{\pi}{8} d_p^2 \rho_f C_D \left(\overrightarrow{V_f} - \overrightarrow{V_p}\right) \left\| \vec{V}_f \right| - \left| \vec{V}_p \right\| \quad , \quad C_D = \frac{24}{Re_p}\left(1 + A Re_p^B\right) + C/\left(1 + D/Re_p\right) \quad , \quad Re_p = \frac{\rho_f}{\mu_f} d_p \left| \vec{V}_f - \vec{V}_p \right| \tag{1}$$

If a particle is sufficiently large and there is a large velocity gradient, there will be a particle lifting force called Saffman force due to fluid shearing forces, which depends on the particle based Reynolds number and the shear flow Reynolds number [8] as follows.

$$\vec{F}_S = \frac{\rho_f \pi}{8} d_p^3 C_{LS} \left(\vec{V}_f - \vec{V}_p\right) \times \nabla \vec{V}_f \quad , \quad C_{LS} = \frac{4.1126}{\sqrt{Re_s}} f\left(Re_p, Re_s\right) \quad , \quad Re_s = \frac{\rho_f}{\mu_f} d_p^2 \left| \vec{\omega}_f \right| \tag{2}$$

The particle inertia forces namely; the centrifugal and Coriolis forces are derived from the second derivative of the vector position. Across a rotating frame the absolute velocity of a particle is changed to the relative velocity. By considering the drag and Saffman force as the main external forces, the following set of second order non-linear differential equations is derived.

$$\begin{cases} \dfrac{\partial^2 r_p}{\partial t^2} = \dfrac{3}{4 d_p} \dfrac{\rho_f}{\rho_p} C_D \sqrt{\left|V_{fr} - V_{pr}\right|^2 + \left|V_{f\theta} - V_{p\theta}\right|^2 + \left|V_{fz} - V_{pz}\right|^2} \left(V_{rf} - V_{rp}\right) + r_p \left(\omega + \dfrac{V_{\theta p}}{r_p}\right)^2 + \dfrac{F_{Sr}}{m_p} \\ \dfrac{\partial^2 \theta_p}{\partial t^2} = \dfrac{3}{4 d_p} \dfrac{\rho_f}{\rho_p} C_D \sqrt{\left|V_{fr} - V_{pr}\right|^2 + \left|V_{f\theta} - V_{p\theta}\right|^2 + \left|V_{fz} - V_{pz}\right|^2} \dfrac{\left(V_{\theta f} - V_{\theta p}\right)}{r_p} - 2 \dfrac{V_{rp}}{r_p} \left(\omega + \dfrac{V_{\theta p}}{r_p}\right) + \dfrac{F_{S\theta}}{r_p m_p} \\ \dfrac{\partial^2 z_p}{\partial t^2} = \dfrac{3}{4 d_p} \dfrac{\rho_f}{\rho_p} C_D \sqrt{\left|V_{fr} - V_{pr}\right|^2 + \left|V_{f\theta} - V_{p\theta}\right|^2 + \left|V_{fz} - V_{pz}\right|^2} \left(V_{zf} - V_{zp}\right) + \dfrac{F_{SZ}}{m_p} \end{cases} \tag{3}$$

The simulation of a particle motion in a turbulent flow requires the determination of the mean and fluctuating flow components which corresponds to a particular eddy and calculated from the local turbulence properties. The turbulence effect is assumed to prevail as long as the particle-eddy interaction time is less than the eddy lifetime and its displacement relative to an eddy is less than the eddy length. The eddy length and lifetime are calculated based on the local turbulence properties of the flow, according to Gosman and Ioannides [10].

Particle tracking through the computational cells requires transforming each particle position into local co-ordinates by solving a set of non-linear equations and updating its position if exceeding the value unity. The flow field data at the representative mesh points are used to interpolate the flow properties during the integration of particle trajectories by Runge-Kutta-Fehlberg seventh order technique. The integration time step is estimated based on the sizes of computational cells and flow velocities, but if a particle interacts with an eddy, the interaction time is considered as the effective time step. Near a boundary condition a more accurate time step is re-evaluated to get an impact within half diameter distance. At a point of impact, the rebound velocity and angle are computed statistically based on the values of mean and standard deviation of the rebound factors derived experimentally by Tabakoff et al. [11] given as polynomial regressions.

$$V_{P2} \Big/ V_{P1} = \sum_{i=0}^{4} a_i \beta_i^i \quad , \quad \beta_{P2} \Big/ \beta_{P1} = \sum_{i=0}^{4} b_i \beta_i^i \tag{4}$$

The particles are released randomly between 0 to 1000 μm (MIL-E5007E distribution) but confirmed to a specified concentration profile. Iterations on particles size and number were repeated till reaching

the convergence in mass. Particle concentrations were varied from a low (50 mg/m$^3$) to a high concentration (1000 mg/m$^3$), and the fan operated at a speed of 1440 rpm for the maximum flow rate.

The intensity and pattern of erosion depend on the physical properties of sand, size, concentration, velocity and angle of impingement, in addition to the geometry and material. The most successful erosion prediction equation directly applied to turbomachinery is that due to Grant and Tabakoff [12] who first generated an erosion model based on aluminium alloy and silica sand as abrasive particles.

$$\varepsilon = K_1 f(\beta_1)(V_{1\theta}^2 - V_{2\theta}^2) + f(V_{1N}) \tag{5}$$

The erosion rate is expressed as the amount of material removed (milligrams) per unit of mass of impacting particles (grams), which depends on the local impact conditions, material and geometry of blades. The values of mass erosion (mg) are calculated from the local erosion rates, and then cumulated and used to compute the equivalent erosion levels in mg/g/cm$^2$.

$$\varepsilon_0 = \frac{1}{A_e \sum_1^N m_{p_i}} \sum_1^N m_{p_i} \varepsilon_i \tag{6}$$

## 4. Results and discussions

Small size particles such as 10 micron (figure 6) tend to follow the flow path and are strongly influenced by the turbulence, secondary flows and flow leakage tip, and are entrained by the large eddy downstream the rotor. For particles of size 100 micron (figure 7) the inertia becomes important, and this why they deviate considerably from flow streamlines through rotor blade and outlet duct. Due to centrifugal forces compared to drag force, large size particles 1000 micron (figure 8) move upwards towards the shroud and keep closer to the outlet wall.

The spread of impacts over the pressure side and on the shroud is shown by figure 9, revealing also the different size of impacting particles and their local velocities and rates of erosion, for which high values are seen upward and over the suction side from leading edge. Large particles tend to impact around the leading edge, whereas the impacts due to small and mid sizes particles are spreading over the pressure side. As revealed the local rates of erosion are low due to low impact velocities which do not exceed 36 m/s. There are several impacts found on the shroud due to the centrifugation. Many particles hitting around the leading edge rebound to reach the blade pressure towards the trailing edge.

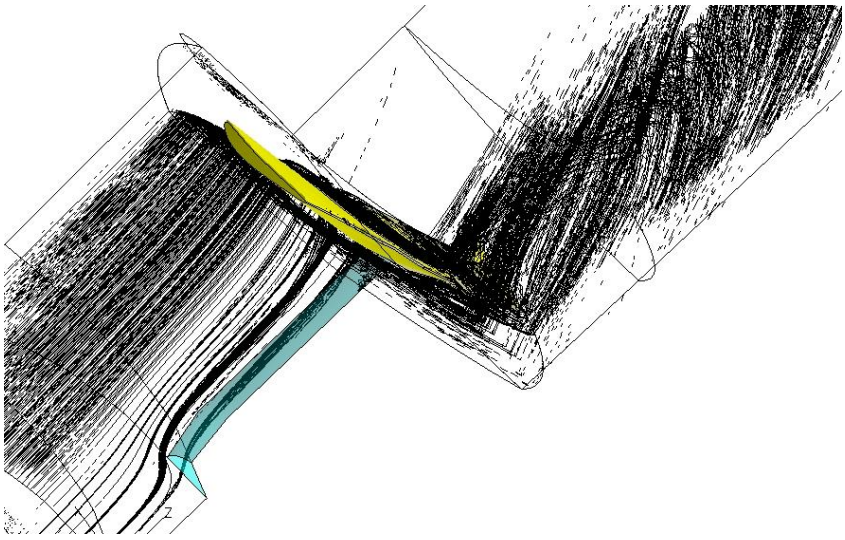

**Figure 6.** Trajectories of 10 micron sand particles

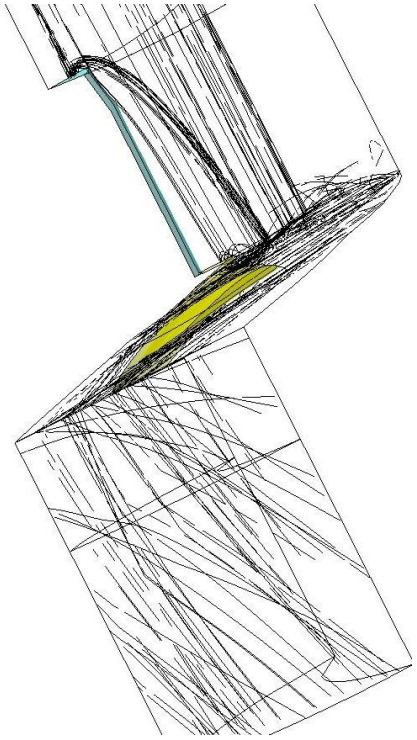

**Figure 7.** Trajectories of 100 micron particles

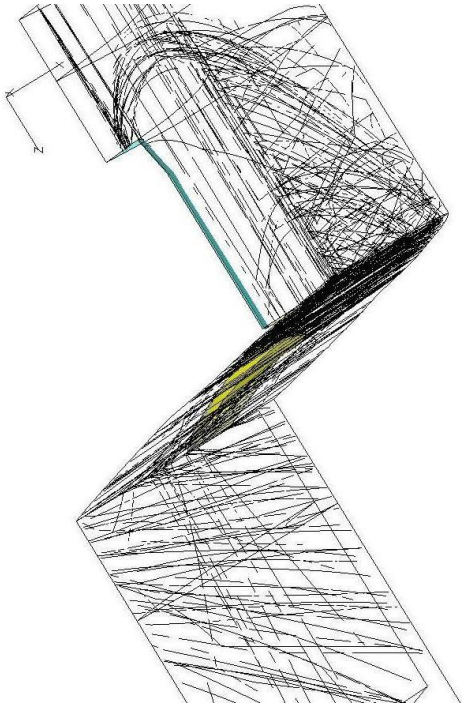

**Figure 8.** Trajectories of 1000 micron particles

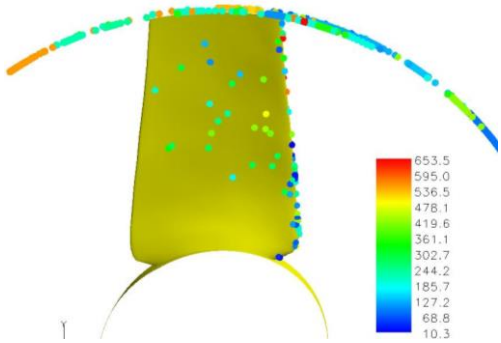


**(a)**

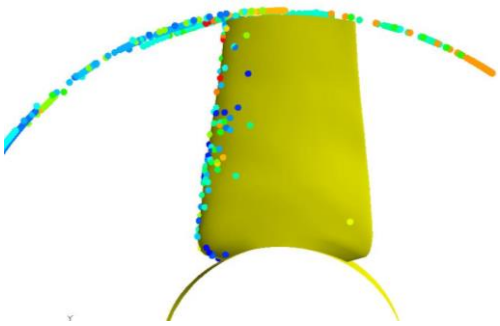

**(b)**

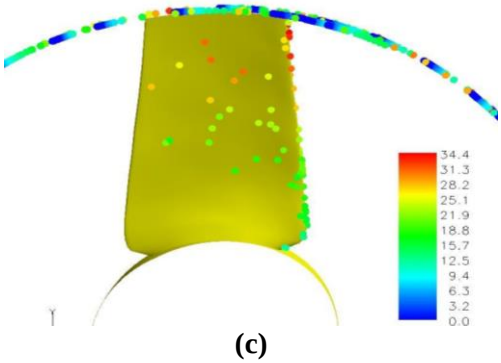


**(c)**

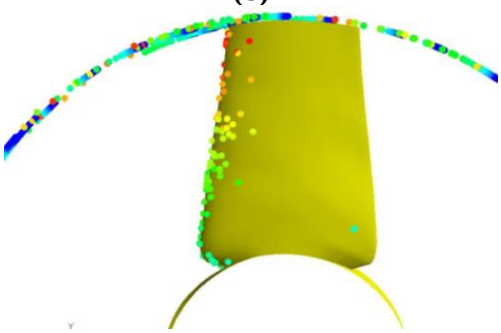

**(d)**

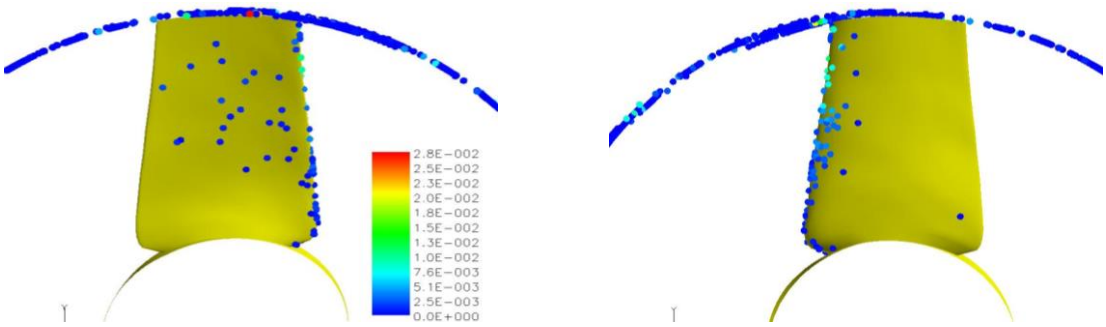


**(e)** **(f)**

**Figure 9.** Sample of impacts with MIL-E5007E sand, left is pressure side and right is suction side, **a-b)** Impact diameter (μm), **c-d)** Impact velocity (m/s), **e-f)** Local erosion (mg/g)

Figure 10 and figure 11 are depicting the predicted erosion patterns corresponding to low concentration and very high concentration. It should be noticed as expected; that these rates of erosion are low for this fan as compared with high speed compressors, because of the low rotational speed 1440 rpm. The predicted erosion patterns are shown to depend largely on the concentration. There is a noticeable erosion of the blade leading edge from root to tip, and over the blade tip and the casing. On the suction side, the erosion is located around the leading edge and expanding towards the tip in a triangular shape. The critical erosion wear is at the top corner from the blade leading edge. On the pressure side, the erosion areas tend to spread, and at the extreme concentration the erosion pattern depicts a rounding of the blade from this side due to material removal. On the shroud the erosion is shown to spread over the tip and downstream trailing edge in scattered areas owing to large impacts encountered, resulting from centrifugal forces and rebound from the rotor. On the hub there are few impacts, mainly near the leading edge.

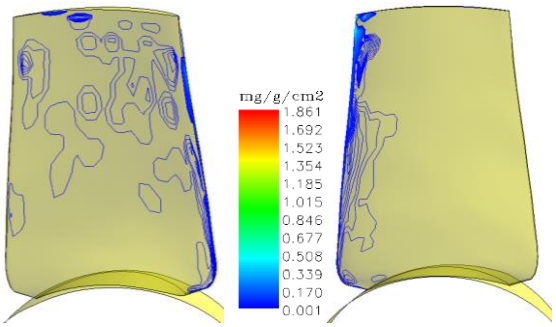


**(a)** **(b)**

**Figure 10.** Equivalent erosion rates (mg/g/cm$^2$) over the blade, due low concentration (50 mg/m$^3$) of MIL-E5007E sand, **a)** pressure side, **b)** suction side

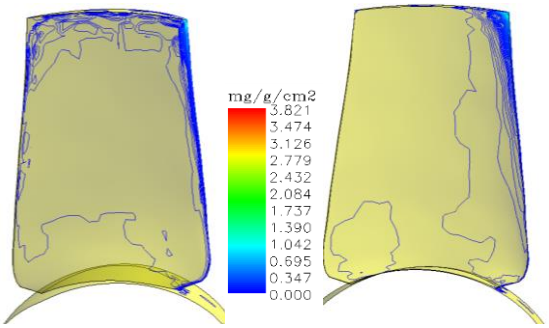


**(a)** **(b)**

**Figure 11.** Equivalent erosion rates (mg/g/cm$^2$) over the blade, due high concentration (1000 mg/m$^3$) of MIL-E5007E sand, **a)** pressure side, **b)** suction side

The results of erosion parameters and blade geometry deterioration after one day of sand particle ingestion are presented in table 1. It is clear that the material removal and geometry changes are related to the mass of particles impacting the blade, concentration and duration of exposure. From the simulations for different operating conditions, one may conclude that the mass erosion from the rotor blade and the shroud increase with the concentration in between 50-1000 mg/m$^3$. The assessed parameters are the mass erosion, overall erosion rate and geometry deterioration estimated as percentages of chord and thickness reduction and plotted in figure 12. It is clear that the material removal and the geometry changes are related to the particle size and concentration and duration of exposure. Accordingly the mass erosion of one blade increases with particle concentration from 2.889

mg to 180.482 mg, which is well illustrated by figure 12(a). Also, it is noticed that the overall erosion rate is almost constant (table 1) and has an average value of $2x10^{-3}$ mg/g. The mass erosion of the shroud (figure 12(b)) is so important and varies with concentration from 4.3 mg to 71.626 mg, whereas that of the hub is extremely lower i.e. from $1.145x10^{-6}$ mg to $1.802x10^{-3}$ mg. The average reduction in blade chord is from $4.175x10^{-4}$ % to $4.054x10^{-3}$ % (table 1 and figure 12(c)), and the thickness from $4.241x10^{-6}$ % to $4.541x10^{-5}$ %, as seen from table 1 and figure 12(d). Also the tip clearance increased from $1.826x10^{-3}$ % to $3.670x10^{-2}$ % according to figure 12(e).

**Table 1.** Erosion and geometry deterioration due to sand ingestion after one day

| Erosion parameters | Concentration (mg/m$^3$) | | | | | | | | | | |
|---|---|---|---|---|---|---|---|---|---|---|---|
| | 50 | 100 | 200 | 300 | 400 | 500 | 600 | 700 | 800 | 900 | 1000 |
| Particle rate (mg/s) | 10.776 | 1.8.0667 | 36.642 | 57.070 | 69.451 | 90.789 | 111.3919 | 128.525 | 142.427 | 166.943 | 180.482 |
| Erosion (mg) | 2.889 | 3.580 | 6.298 | 9.253 | 11.190 | 15.3015 | 18.983 | 20.849 | 24.727 | 29.777 | 30.848 |
| Reduction in mass (%) | 7.272E-04 | 9.009E-04 | 1.584E-03 | 2.328E-03 | 2.815E-03 | 3.850E-03 | 4.777E-03 | 5.246E-03 | 6.222E-03 | 7.493E-03 | 7.762E-03 |
| Overall erosion rate (mg/g) | 3.104E-03 | 2.293E-03 | 1.989E-03 | 1.675E-03 | 1.725E-03 | 1.950E-03 | 1.972E-03 | 1.877E-03 | 2.009E-03 | 2.064E-03 | 1.978-03 |
| Blade length reduction (%) | 4.175E-04 | 4.276E-04 | 9.007E-04 | 1.477E-03 | 1.739E-03 | 2.341E-03 | 2.784E-03 | 3.062E-03 | 3.428E-03 | 3.934E-03 | 4.054E-03 |
| Thickness reduction (%) | 4.241E-06 | 5.103E-06 | 9.436E-06 | 1.564E-05 | 1.693E-05 | 2.375E-05 | 2.841E-05 | 3.127E-05 | 3.663E-05 | 4.284E-05 | 4.541E-05 |
| Tip clearance Increase (%) | 1.826E-03 | 3.708E-03 | 7.842E-03 | 9.449E-03 | 1.217E-02 | 1.326E-02 | 1.618E-02 | 1.902E-02 | 2.082E-02 | 2.783E-02 | 3.670E-02 |
| Erosion of hub (mg) | 1.145E-06 | 7.648E-03 | 1.680E-05 | 5.467E-04 | 4.077E-04 | 3.250E-04 | 7.185E-04 | 8.292E-04 | 6.442E-03 | 6.035E-04 | 1.802-03 |
| Erosion of shroud (mg) | 4.300 | 6.965 | 12.261 | 20.748 | 25.706 | 33.198 | 38.317 | 48.342 | 51.565 | 63.423 | 71.626 |

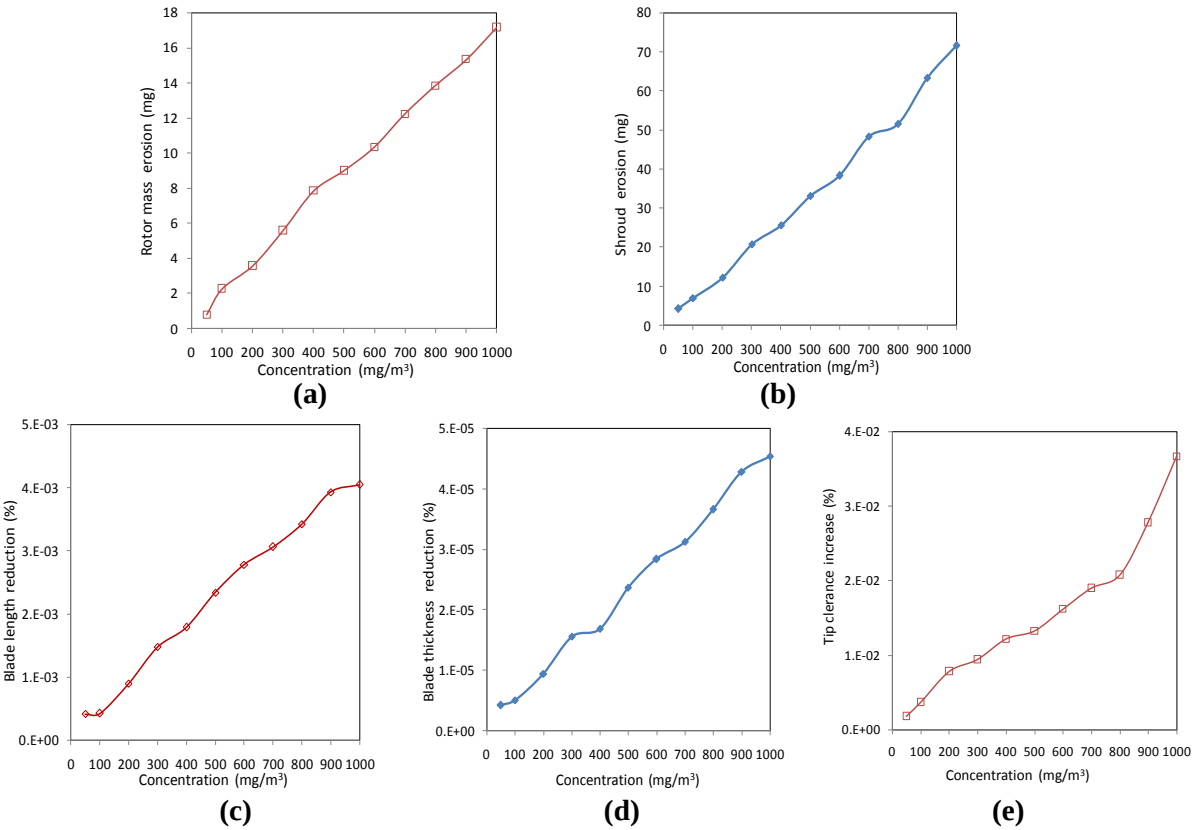


**Figure 12.** Erosion degradations after one week of sand ingestion: **a)** Blade erosion, **b)** shroud erosion, **c)** Blade length reduction, **d)** Blade thickness reduction, **e)** Tip clearance increase

As exhibited by figure 13, the erosion phenomenon is shown to distort the leading edge and reduce the chord and thickness of blade, progressively from mid span to tip. The process of erosion is more likely to cut the fore of tip section and the thickness is changing. In addition, the distortion at leading edge affects the flow circulation and moves the stagnation point, which should alter the static pressure distribution and its aerodynamic quality.

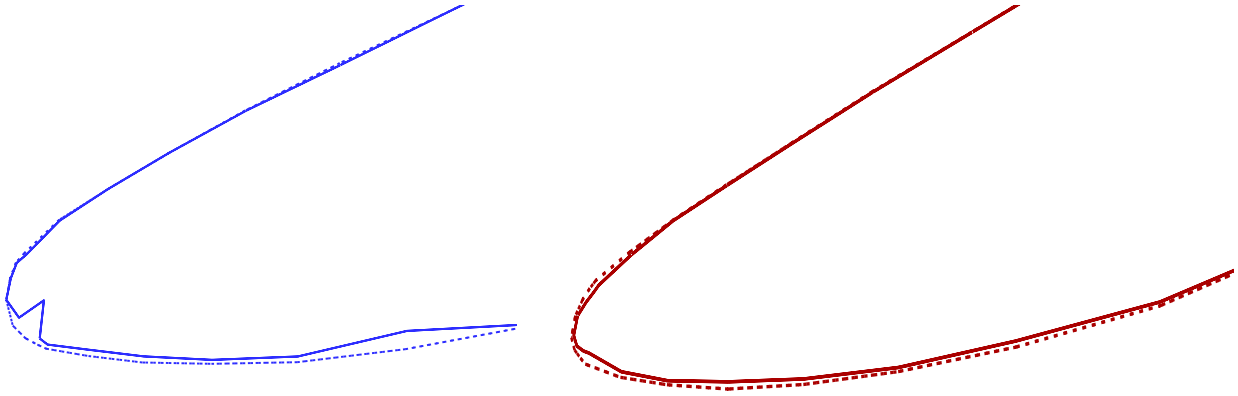

**(a)** **(b)**

**Figure 13.** Eroded profiles, **a)** Tip profile **b)** Mid-span profile

## 5. Conclusion

High impacts and erosion rates are predicted around the leading edge of the rotor blade due to its direct exposure to incoming sand particles. Impacts on the suction side are related to particles entering the rotor blades at high negative angle of direction. Impacts on the remainder of the pressure side are due to flow condition at the rotor entrance and rebounds around the leading edge. On the shroud, the impacts and erosion are connected to the particles acquiring centrifugal forces. On the hub there are few impacts. In general, the obtained rates of erosion are lower compared to high speed compressors. The consequent amount of predicted erosion data may help assessing fans of similar design operating in polluted environments, as well as envisaging adequate coating for the critical eroded area to extend the time of life.

## Nomenclature

| | |
|---|---|
| A | Area ($m^2$) |
| C | Concentration ($mg/m^3$) |
| $C_D$ | Drag coefficient |
| $C_L$ | Lift coefficient |
| d | Diameter (m) |
| $K_1$ | Material constant |
| m | Mass (kg) |
| P | Pressure (Pa) |
| r | Radius, radial co-ordinate (m) |
| t | Time (s) |
| U | Peripheral velocity (m/s) |
| V | Absolute velocity (m/s) |
| W | Relative velocity (m/s) |
| z | Axial co-ordinate (m) |

Greek letters

| | |
|---|---|
| $\beta$ | Impact angle (deg) |
| $\varepsilon$ | Erosion rate (mg/g) |
| $\varepsilon_\rho$ | Equivalent erosion rate ($mg/g/cm^2$) |

| | |
|---|---|
| $\rho$ | Density (kg/m$^3$) |
| $\omega$ | Speed of rotation rad/s |
| $\theta$ | Angular position (rad) |

Subscript

| | |
|---|---|
| D | Drag |
| f | Fluid |
| N | Normal |
| p | Particle, pressure |
| r | Radial |
| $\theta$ | Tangential component |
| S | Saffman |
| z | Axial direction |
| 1,2 | At impact and rebound from a surface |

**References**

**[1]** Tabakoff W 1984 Review of Turbomachinery performance Deterioration Exposed to Solid Particulate Environment, *ASME Journal of Fluids Engineering*, Vol 106, June 1984 , pp125–134

[2] Balan C and Tabakoff W 1984 Axial Flow Compressor Performance Deterioration, *AIAA paper 84-1208*, June 1984

[3] Ghenaiet A, Tan S C and Elder R L 2004 Experimental Investigation of an Axial Fan Erosion and Performance Degradation, *IMechE Journal of Power and Energy*, September 2004 Vol. 218 N. A6, ISSN : 0957-6509

[4] Hussein M F and Tabakoff W 1974 Computation and Plotting of Solid Particle Flow in Rotating Cascades, *J Computers and Fluids*, Vol. 2, No. 1, 1974, pp. 1–15.

[5] Ghenaiet A, Tan, S C and Elder, R L 2005 Prediction of an Axial Turbomachine Performance Degradation *IMechE Journal of Power and Energy*, June 2005 Vol. 219 N. A 4, ISSN: 0957-6509

[6] Ghenaiet A 2009 Simulation of Sand Particles Ingestion Through a Cooling Fan, IMechE, *Compressors and Their Systems 2009 paper L20/C682/056*, Chandos Publishing Oxford 2009**,** ISBN 978-1-84334-581-7

[7] Ghenaiet A 2005 Numerical Simulations of Flow and Particle Dynamics within a Centrifugal Turbomachine, *Compressors and Their Systems 2005*, *IMechE paper C639_52*, ISBN: 0-470-02576-X Wiley publisher

[8] Sommerfeld M 2000 Theoretical and Experimental Modelling of Particulate Flow - Overview and Fundamentals, *VKI Lecture series* 2000–06, April 3-7 2000, Von Karman Institute, Belgium

[9] Haider A and Levenspiel O 1989 Drag Coefficient and Terminal Velocity of Spherical and non Spherical Particles, *J Powder Technology*, 58 (1989) 63.

[10] Gosman A D and Ionnides E 1981 Aspects of Computer Simulation of Liquid Fuelled Combustors, *AIAA 19$^{th}$ Aerospace Science Meeting St Louis Missouri*, paper AIAA 81-0323

[11] Tabakoff W, Hamed A and Murugan D M 1996 Effect of Target Materials on the Particle Restitution Characteristics for Turbomachinery Application, *Journal of propulsion and power* Vol. 12 No2, March-April 1996

[12] Grant G and Tabakoff W 1975 Erosion Prediction in Turbomachinery Resulting from Environmental Particles, *AIAA Journal of Aircraft*, Vol. 12, No. 5, 1975, pp. 471–478.